Control of ultracold atoms with a chiral ferromagnetic film

Ren Qin and Yong Wang*
School of Physics, Nankai University, Tianjin 300071, China

(Received 18 July 2018; revised manuscript received 19 November 2018; published 2 January 2019)

We show that the magnetic field produced by a chiral ferromagnetic film can be applied to control ultracold atoms. The film will act as a magnetic mirror or a reflection grating for ultracold atoms when it is in the helical phase or the skyrmion crystal phase, respectively. By applying a bias magnetic field and a time-dependent magnetic field, one-dimensional or two-dimensional magnetic lattices including honeycomb, Kagome, and triangular types can be created to trap the ultracold atoms. We have also discussed the trapping height, the potential barrier, the trapping frequency, and the Majorana loss rate for each lattice. Our results suggest that the chiral ferromagnetic film can be a platform to develop artificial quantum systems with ultracold atoms based on modern spintronics technologies.

DOI: 10.1103/PhysRevA.99.013401

I. INTRODUCTION

In the past three decades, ultracold atomic physics has been greatly developed with progressive techniques to cool, trap, and manipulate neutral atoms with electromagnetic fields [1,2]. The quantum nature of the ultracold atomic gases will emerge after suppressing the thermal fluctuations, and these artificially controllable quantum systems provide the ideal platforms for realizing Bose-Einstein condensation, simulating quantum many-body phenomena, performing quantum computation, designing atomic interferometers, etc. Two typical mechanisms to control the neutral atoms are the alternating-current Stark energy shift in the high-frequency optical field and the Zeeman energy shift in the inhomogeneous magnetic field. The former has been widely applied to construct optical lattices for ultracold atoms, which play a crucial role in the design of various quantum simulators [3], while the latter lays the foundation to design and develop atom chips [4]. In fact, the two mechanisms are more often combined together to achieve the best level of control of the ultracold atoms.

Several strategies have been developed to produce the desirable magnetic field to control ultracold atoms. The most flexible approach is to fabricate current-carrying conductive microstructures to generate the Oersted field, which has been applied to guide and trap ultracold atoms in various configurations [5]. This approach however suffers from the Johnson thermal noise and wire roughness for miniature devices. Another alternative way is to utilize the permanent ferromagnetic film with artifical patterns as the effective "magnetization current" [6,7], which however is hard to be reconfigured and switched off. Besides, there also exist other theoretical proposals to generate magnetic lattice for ultracold atoms, such as the vortex array in superconducting films [8,9] and time-periodic magnetic field pulses [10,11].

In addition to artificial patterns, noncollinear magnetic textures can also induce inhomogeneous configurations of the magnetic field near the surface of the ferromagnetic film. Indeed, West *et al.* have demonstrated the ability to manipulate ultracold ^{87}Rb atoms by magnetic domain walls in planar magnetic nanowires [12]. Recently, chiral ferromagnetic materials with finite Dzyaloshinskii-Moriya interaction (DMI) resulting from a lack of spatial inversion symmetry [13,14] have attracted broad research interests [15,16], mainly due to the discovery of magnetic skyrmions therein [17–22] and the promising applications to develop spintronics devices [23,24]. With the formation of magnetic skyrmions, the magnetic field distribution near the surface of the chiral ferromagnetic film will also have been modified. For example, the magnetic field produced by an isolated magnetic skyrmion has been measured with the nitrogen-vacancy center in diamond [25]. The magnetic field distributions generated by the magnetic skyrmion crystals (SkXs) with different helicity have also been investigated theoretically [26]. Therefore, it will be interesting to examine the possibility to control the ultracold atoms with the magnetic field produced by a chiral ferromagnetic film.

In this paper, we show that a chiral ferromagnetic film can be utilized to design magnetic mirrors, reflection grating, magnetic lattices, etc., which are the elementary devices to control ultracold atoms. Considering the diversity of chiral ferromagnetic materials and the rapidly developing spintronics techniques, the approach proposed here could be crucial to developing ultracold atom physics in the future.

II. BASIC PRINCIPLE AND MODEL

The proposed device is schematically shown in Fig. 1(a). A chiral ferromagnetic film is placed in the x-y plane with $z = 0$ nm, which will generate the spatial distributions of the magnetic field $\boldsymbol{\mathcal{B}}_c$. A uniform magnetic field, $\boldsymbol{\mathcal{B}}_0$, is applied perpendicular to the film to create zero points at finite heights. Furthermore, a time-dependent magnetic field, $\boldsymbol{\mathcal{B}}_M = \mathcal{B}_M(\sin\omega_M t, \cos\omega_M t, 0)$, parallel to the film will be

*yongwang@nankai.edu.cn

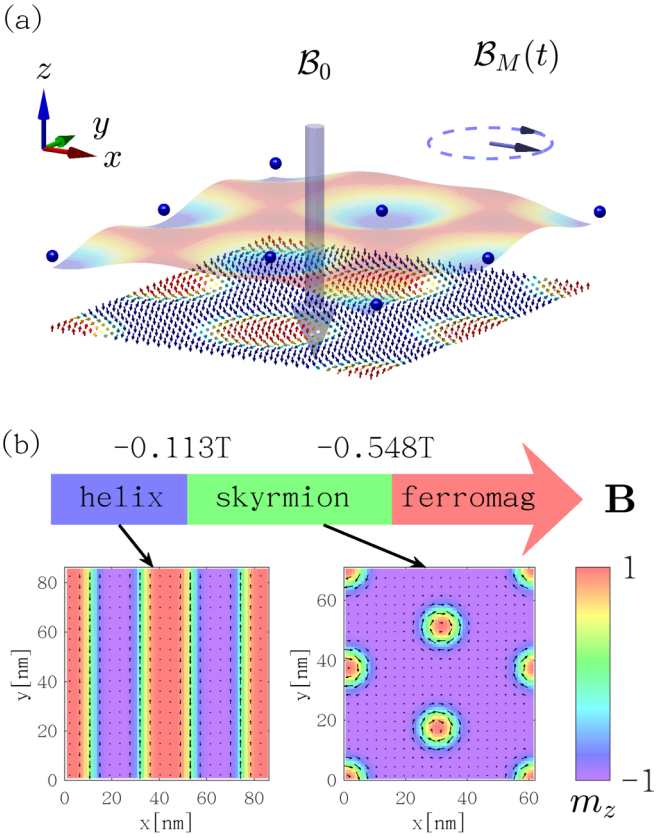

FIG. 1. (a) Schematic diagram for the device. A chiral ferromagnetic film with prepared magnetization configuration is placed at the x-y plane with $z = 0$ nm, which will produce a magnetic field, $\boldsymbol{\mathcal{B}}_c$. A bias magnetic field, $\boldsymbol{\mathcal{B}}_0$, is applied perpendicular to the film, and a time-dependent magnetic field, $\boldsymbol{\mathcal{B}}_M(t)$, is applied parallel to the film. The trapping potential for the ultracold atoms (blue balls) is a combination of the three magnetic fields. (b) Phase transition of the chiral ferromagnetic film defined by Eq. (1). The magnetization configurations of the helical phase and the skyrmion crystal phase are obtained at $\mathbf{B} = 0$ T and $\mathbf{B} = -(0, 0, 0.3)$ T, respectively. The arrows denote the magnetization direction at each site, and the amplitude of m_z is shown with different colors.

introduced to generate an effective time-orbiting potential in order to suppress the Majorana loss [9,27]. Thus, the total magnetic field profile of such a device will be $\boldsymbol{\mathcal{B}} = \boldsymbol{\mathcal{B}}_c + \boldsymbol{\mathcal{B}}_0 + \boldsymbol{\mathcal{B}}_M$.

When an atom with the magnetic dipole moment $\boldsymbol{\mu}$ is moving in the inhomogeneous magnetic field $\boldsymbol{\mathcal{B}}(\mathbf{r})$, it will experience the Stern-Gerlach force given by the potential energy $U(\mathbf{r}) = -\boldsymbol{\mu} \cdot \boldsymbol{\mathcal{B}}(\mathbf{r})$. If the spatial change of the magnetic field felt by the atom is much slower than its Larmor precession, its magnetic moment will adiabatically follow the direction of the magnetic field, and the potential energy will now depend only on the modulus of $\boldsymbol{\mathcal{B}}(\mathbf{r})$, which is given as $U(\mathbf{r}) = m_F g_F \mu_B \mathcal{B}(\mathbf{r})$ for the hyperfine state $|F, m_F\rangle$ [4]. Here, g_F is the Landé factor, μ_B is the Bohr magneton, F is the total angular momentum quantum number, and m_F is the magnetic quantum number of the atom. Therefore, the atom will be in the strong-field seeking state for $m_F g_F < 0$ and in the weak-field seeking state for $m_F g_F > 0$. Since no minimum can exist in the potential $U(\mathbf{r})$ for the strong-field seeking state according to the Earnshaw's theorem [4], only the atoms prepared in the weak-field seeking state can be magnetically trapped. For example, the ^{87}Rb and ^{7}Li atoms can be magnetically trapped when they stay in the state $|F = 2, m_F = 2\rangle$ [5,28].

The external magnetic field $\mathbf{B}$ should be applied *in advance* to tune the magnetization configuration of the chiral ferromagnetic film, which is described by the energy functional density

$$\mathcal{E}[\mathbf{m}] = \frac{J}{2}(\nabla \mathbf{m})^2 + D\mathbf{m} \cdot (\nabla \times \mathbf{m}) - K\mathbf{m}_z^2 - M_s \mathbf{B} \cdot \mathbf{m}. \tag{1}$$

Here, $\mathbf{m}(\mathbf{r})$ is the magnetization distribution of the film normalized by the saturation magnetization M_s; the four terms in Eq. (1) are the Heisenberg exchange interaction, the DM interaction, the perpendicular magnetic anisotropy energy, and the Zeeman energy in the presence of the applied magnetic field $\mathbf{B}$, respectively. Then the magnetization dynamics are given by the Landau-Lifshitz-Gilbert(LLG) equation

$$\frac{d\mathbf{m}}{dt} = -\gamma \mathbf{m} \times \mathbf{H}^{\text{eff}} + \alpha \mathbf{m} \times \frac{d\mathbf{m}}{dt}. \tag{2}$$

Here, γ is the gyromagnetic ratio, $\mathbf{H}^{\text{eff}} = -\frac{1}{M_s}\nabla_{\mathbf{m}}\mathcal{E}[\mathbf{m}]$ is the effective magnetic field, and α is the Gilbert damping coefficient. For a given set of parameters, the stable magnetization configuration of the chiral ferromagnetic film is achieved as the stationary solution of the LLG equation [26]. As shown in Fig. 1(b), when the external magnetic field $\mathbf{B}$ is perpendicular to the film and is continuously increased from zero, the ground state of the chiral ferromagnetic film will evolve from the helical phase to the skyrmion crystal phase at first and reach the ferromagnetic phase finally. During the micromagnetic simulations, the parameters are set as $J = 15$ pJ/m, $D = 3$ mJ/m^2, $K = 0.7$ mJ/m^3, $M_s = 580$ kA/m, $\alpha = 0.3$, and the thickness of the film is assumed to be 1 nm. The film is subdivided into cubic grids with the size $1 \times 1 \times 1$ nm^3, and the time step for the simulations is set as 0.01 ps. Besides, the temperature is linearly decreased from 1000 to 0 K during 100 ns to avoid possible local minima trap.

The external magnetic field $\mathbf{B}$ will be withdrawn once the desirable magnetization pattern is stably reached. Then the magnetic field $\boldsymbol{\mathcal{B}}_c(\mathbf{r})$ generated by the magnetization configuration $\mathbf{m}(\mathbf{r})$ of the chiral ferromagnetic film can be directly calculated as [26]

$$\boldsymbol{\mathcal{B}}_c(\mathbf{r}) = \frac{\mu_0}{4\pi} \int d\mathbf{r}' \frac{3(\mathbf{m}(\mathbf{r}') \cdot \hat{\boldsymbol{\mathcal{R}}})\hat{\boldsymbol{\mathcal{R}}} - \mathbf{m}(\mathbf{r}')}{\mathcal{R}^3}, \tag{3}$$

where $\boldsymbol{\mathcal{R}} = \mathbf{r} - \mathbf{r}'$. Below, we study how to control the ultracold atoms in the weak-field seeking state with the magnetic field $\boldsymbol{\mathcal{B}}_c(\mathbf{r})$ when the chiral ferromagnetic film is prepared in the helical phase and the skyrmion crystal phase, respectively.

III. HELICAL PHASE

As shown in Fig. 1(b), the helical phase can be achieved as the ground state of the chiral ferromagnetic film when $\mathbf{B} = 0$, where the magnetization configuration is periodically modulated in one direction and mimics the structure of a magnetic mirror for ultracold atoms fabricated from permanent ferromagnetic materials [4,29]. Nevertheless, it is advantageous

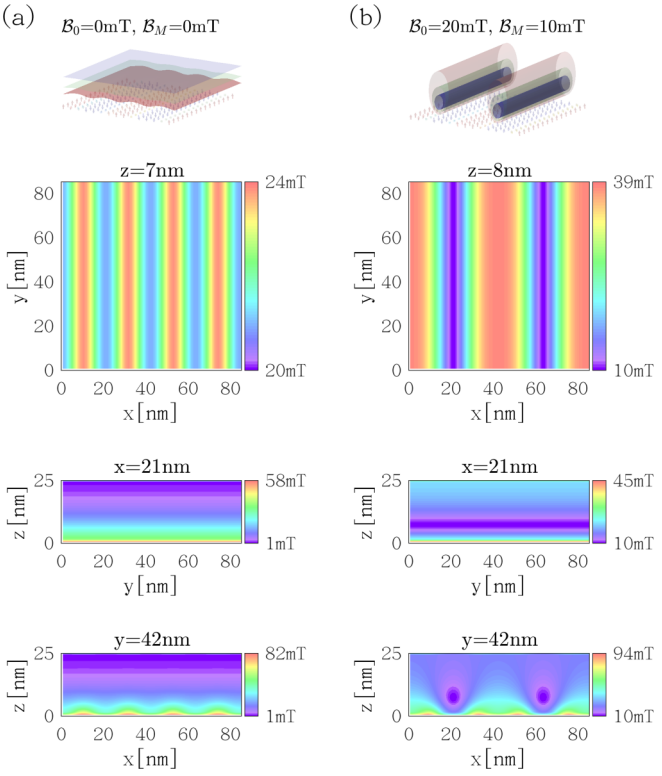

FIG. 2. Profiles of the magnetic field amplitude $\mathcal{B}(\mathbf{r})$ for a chiral ferromagnetic film at the helical phase. (a) Magnetic mirror when $\mathcal{B}_0 = 0\,\mathrm{mT}$ and $\mathcal{B}_M = 0\,\mathrm{mT}$. Top panel: Isosurfaces of $\mathcal{B}(\mathbf{r})$ with three values: 8, 16, and 24 mT. Middle and bottom panels: Cross sections of $\mathcal{B}(\mathbf{r})$ when $z = 7$ nm, $x = 21$ nm, and $y = 42$ nm, respectively. (b) One-dimensional magnetic lattice when $\mathcal{B}_0 = 20$ mT and $\mathcal{B}_M = 10$ mT. Top panel: Isosurfaces of $\mathcal{B}(\mathbf{r})$ with three values: 13.5, 17.0, and 20.5 mT. Middle and bottom panels: Cross sections of $\mathcal{B}(\mathbf{r})$ when $z = 8$ nm, $x = 21$ nm, and $y = 42$ nm, respectively.

to utilize a chiral ferromagnetic film in the helical phase as a magnetic mirror, since the helical phase is spontaneously formed as the ground state and can also be easily switched off by applying an external magnetic field. Here, the complex fabrication processes are not required in comparison to the ferromagnetic film with artificial patterns [4,29]. Besides, the period of the helical phase can be tuned by engineering the DMI [30,31], which thereby makes it flexible to control ultracold atoms.

The magnetic field amplitude $\mathcal{B}_c(\mathbf{r})$ solely generated by the chiral ferromagnetic film in the helical phase in Fig. 1(b) has been numerically calculated based on Eq. (3) and is demonstrated in Fig. 2(a). Here, the bias magnetic field $\boldsymbol{\mathcal{B}}_0$ and the time-dependent field $\boldsymbol{\mathcal{B}}_M$ have not been switched on yet. We see that the isosurfaces of $\mathcal{B}_c(\mathbf{r})$ will be nearly parallel to the x-y plane. In fact, a weak periodic modulation of $\mathcal{B}_c(\mathbf{r})$ will happen at fixed height z. For example, $\mathcal{B}_c(\mathbf{r})$ will periodically vary from 21 to 24 mT when $z = 7$ nm. On the other hand, $\mathcal{B}_c(\mathbf{r})$ will decay from 81 to 2 mT when the height z increases from 0 to 25 nm. Therefore, the effective distance for a chiral ferromagnetic film to control the ultracold atoms will be tens of nanometers with the given simulation parameters here.

The simulated results in Fig. 2(a) can be further understood considering that the magnetization configuration of the helical phase can be approximated as a single-$\mathbf{Q}$ state $\mathbf{m}_h(\mathbf{r}) = \mathbf{m}_0\delta(z) + \mathcal{A}[\hat{\mathbf{e}}_z \cos(\mathbf{Q}\cdot\mathbf{r}) + \hat{\mathbf{e}}\sin(\mathbf{Q}\cdot\mathbf{r})]\delta(z)$. Here, $\hat{\mathbf{e}}_z$ is the unit vector normal to the film and $\mathbf{Q}$ defines the wave vector of the helical state; the unit vector $\hat{\mathbf{e}}$ is determined as $\hat{\mathbf{e}} = \hat{\mathbf{e}}_z \times \hat{\mathbf{Q}}$ for the Bloch-type DMI given in Eq. (1); $\mathcal{A}$ gives the amplitude of the modulated magnetization configuration of the helical state. The delta function $\delta(z)$ here implies that the thickness of the film is neglected. Then the magnetic field distribution $\boldsymbol{\mathcal{B}}_h(\mathbf{r})$ generated by the single-$\mathbf{Q}$ state $\mathbf{m}_h(\mathbf{r})$ is analytically obtained as [26]

$$\boldsymbol{\mathcal{B}}_h(\mathbf{r}) = \frac{\mathcal{A}Q}{2} e^{-Q|z|}[\mathrm{sgn}(z)\hat{\mathbf{Q}}\sin(\mathbf{Q}\cdot\mathbf{r}) + \hat{\mathbf{e}}_z\cos(\mathbf{Q}\cdot\mathbf{r})], \tag{4}$$

and its modulus is $\mathcal{B}_h(\mathbf{r}) = \frac{\mathcal{A}Q}{2}e^{-Q|z|}$. Therefore, the chiral ferromagnetic film described by the single-$\mathbf{Q}$ state will establish an exponential repulsive potential to reflect the ultracold atoms in the weak-field seeking state. The decay length of the potential is proportional to the period of the helical phase, which is usually about a few tens of nanometers or even smaller for typical chiral ferromagnetic materials [23]. Since the period and the decay length of the artificial microstructures are usually in the order of magnitude of micrometers [4], a much harder magnetic mirror for ultracold atoms can be realized with the chiral ferromagnetic film. Note that $\mathcal{B}_h(\mathbf{r})$ here is constant at the given height z, which is different from the numerical result in Fig. 2(a). This minor deviation originates from the magnetic anisotropy energy in Eq. (1), where the single-$\mathbf{Q}$ state becomes an oversimplified and inaccurate description of the helical phase. It will be important to choose the materials with smaller magnetic anisotropy to get more smooth mirrors.

The profile of magnetic field amplitude will be modified significantly when the bias magnetic field $\boldsymbol{\mathcal{B}}_0$ and the time-dependent magnetic field $\boldsymbol{\mathcal{B}}_M$ are turned on [4,29]. Figure 2(b) shows the distribution of total magnetic field amplitude $\mathcal{B}(\mathbf{r})$ for the device when $\boldsymbol{\mathcal{B}}_0 = (0, 0, 20)$ mT and $\mathcal{B}_M = 10$ mT. As shown in Fig. 2(b), the minima of $\mathcal{B}(\mathbf{r})$ in this case will locate at the parallel lines in the plane $z = 8$ nm, and the appearing one-dimensional magnetic lattice is able to trap the ultracold atoms in the weak-field seeking state. We can define the "recoil energy" of the lattice as $E_R = \pi^2\hbar^2/(2m_a a^2)$, where m_a is the atomic mass and a is the lattice constant [9]. For the helical phase with $a = 42$ nm here, the recoil energy E_R is estimated as 1.3 neV for the ^{87}Rb atom or 16 neV for the ^{7}Li atom, respectively.

The numerical results in Fig. 2(b) can also be understood with the help of the single-$\mathbf{Q}$ state. Assuming that $\boldsymbol{\mathcal{B}}_0 = \frac{\mathcal{A}Q}{2}(0, 0, B_0)$ and $\mathcal{B}_M = \frac{\mathcal{A}Q}{2}B_M$, the modulus of the total magnetic field $\boldsymbol{\mathcal{B}}(\mathbf{r})$ will be

$$\mathcal{B}(\mathbf{r}) = \frac{\mathcal{A}Q}{2}\sqrt{B_0^2 + B_M^2 + e^{-2Q|z|} + 2B_0 e^{-Q|z|}\cos(\mathbf{Q}\cdot\mathbf{r})}. \tag{5}$$

Therefore, such an operation will create a one-dimensional periodic potential for the ultracold atoms in the plane parallel to the film. This in fact forms an effective reflection grating

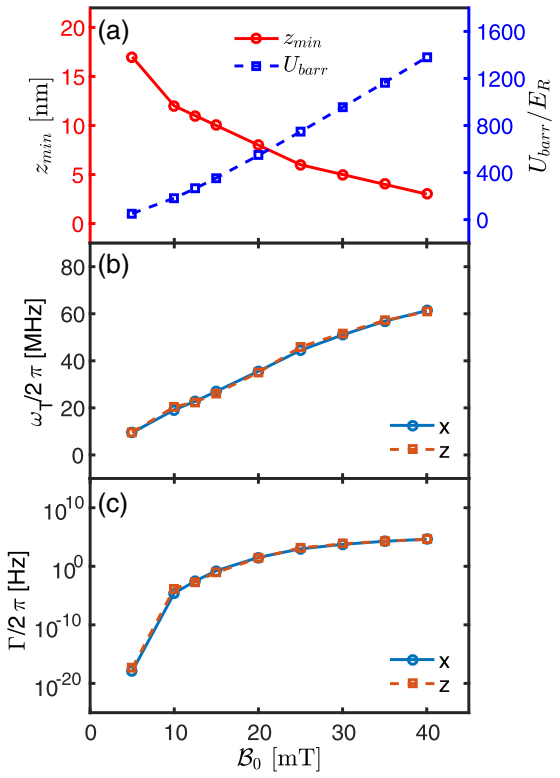

FIG. 3. Field-dependent parameters of the one-dimensional magnetic lattice for the ^{87}Rb atom. (a) The trapping height $z_{\min}$ and the potential barrier $U_{\rm barr}$ in the unit of the recoil energy E_R. (b) The trapping frequency $\omega_T/2\pi$. (c) The Majorana loss rate $\Gamma/2\pi$. Here, $\mathcal{B}_0$ varies from 5 to 40 mT, while $\mathcal{B}_M$ is fixed as 10 mT.

for the incident atoms [29], which will attain the period in the range of nanometers and hence greatly extend the border of current technologies. Furthermore, the modulus $\mathcal{B}(\mathbf{r})$ will achieve its minimal value $\mathcal{B}_{\min} = \mathcal{B}_M$ along the parallel lines defined by $\cos(\mathbf{Q}\cdot\mathbf{r}_{\min}) = -1$ and $|z_{\min}| = -\frac{1}{Q}\ln B_0$ in the case of $B_0 < 1$. Thus, the magnetic field around each line will become a guide to trap the ultracold atoms, where the trapping height $|z_{\min}|$ depends on the applied magnetic field. When $\mathcal{B}_0$ is continuously increased, the guides will get close to the film and finally disappear at $B_0 = 1$. This trend has also been verified in the numerical calculations, as shown in Fig. 3(a). When the magnetic field $\mathcal{B}_0$ varies from 5 to 40 mT, the trapping height of the one-dimensional magnetic lattice will decay from about 17 to 3 nm.

In addition to the trapping height, the potential barrier for the atoms to escape from the minima locations $z_{\min}$ to the infinitely far region $z \to \infty$ can also be tuned by the magnetic field $\boldsymbol{\mathcal{B}}_0$. The difference between the magnetic field amplitudes $\mathcal{B}(\infty)$ and $\mathcal{B}(z_{\min})$ will be $\delta\mathcal{B} = \sqrt{\mathcal{B}_0^2 + \mathcal{B}_M^2} - \mathcal{B}_M$, and the potential barrier will be $U_{\rm barr} = m_F g_F \mu_B \delta\mathcal{B}$. When $\mathcal{B}_M$ is fixed as 10 mT and $\mathcal{B}_0$ increases from 5 to 40 mT, the potential barrier for the ^{87}Rb and ^{7}Li atoms in the $|F = 2, m_F = 2\rangle$ state will vary from 0.068 to 1.81 μeV, which corresponds to the temperature range from 0.8 to 21 mK. In Fig. 3(a), the dependence of $U_{\rm barr}$ on $\mathcal{B}_0$ is explicitly shown in the unit of the recoil energy E_R for the ^{87}Rb atom.

The trapping frequency ω_T of the atoms near the minima of the one-dimensional magnetic lattice can be calculated as $\omega_T = \sqrt{m_F g_F \mu_B \mathcal{B}''_{\min}/m_a}$, where $\mathcal{B}''_{\min}$ is the magnetic field curvature at the minima. Figure 3(b) shows the trapping frequencies along the x and z directions for the ^{87}Rb atom in $|F = 2, m_F = 2\rangle$ state when $\mathcal{B}_M = 10$ mT and $\mathcal{B}_0 \in [5, 40]$ mT, where $\omega_{T,x}/2\pi \in [9.5, 61.3]$ MHz and $\omega_{T,z}/2\pi \in [9.7, 60.9]$ MHz, respectively. Then the energy of the ^{87}Rb atom will be in the range [0.04, 0.25] μeV, which corresponds to the temperature range [0.46,2.9] mT. Since the mass of the ^{7}Li atom is about one-twelfth of the ^{87}Rb atom's mass, its trapping frequency will be about 3.5 times of the estimated value above.

The Majorana loss rate near the minima of the lattice potential can be estimated as $\Gamma/2\pi = \omega_T \exp(-4\omega_L/\omega_T)$ [9,32], where $\omega_L = m_F g_F \mu_B \mathcal{B}_M/\hbar$ is the Larmor precession frequency at the minima. As shown in Fig. 3(c), $\Gamma/2\pi$ for the ^{87}Rb atom will increase from 10^{-18} to 10^4 Hz when the magnetic field $\mathcal{B}_0$ varies from 5 to 40 mT. Therefore, for a given $\mathcal{B}_M$, the magnetic field $\mathcal{B}_0$ will give a higher potential barrier $U_{\rm barr}$ and a larger Majorana loss rate $\Gamma/2\pi$ simultaneously, which should be optimally chosen during practical applications. Besides, the Majorana loss rate for the ^{7}Li atom will be larger because of its higher trapping frequency in the lattice.

More complex potential profiles for ultracold atoms can be constructed based on the helical phase in the chiral ferromagnetic film. For example, if the applied magnetic field is along the magnetic stripes of the helical phase, the reflection plane of the magnetic mirror will be shifted toward the film [29]. Then a vibrating magnetic mirror for the ultracold atoms can be realized if the applied field is harmonically oscillated [29]. Furthermore, a "moving grating" or "conveyor belt" [29] can be obtained if a magnetic field is rotating in the plane perpendicular to the magnetic stripes. Therefore, we expect that the helical phase in a chiral ferromagnetic film can have widespread applications to develop and design various elementary devices for atom optics and atom chips.

IV. SKYRMION CRYSTAL PHASE

The chiral ferromagnetic film can be driven into the SkX phase by a strong magnetic field $\mathbf{B}$, as shown in Fig. 1(b). Due to its topologically protected nature, the SkX phase will exist as a metastable state after withdrawing the applied magnetic field [33]. The lifetime of the metastable SkX phase there can be as long as 10^4 s at 23 K [33], which is long enough to manipulate the ultracold atoms. The magnetic field distributions generated by Bloch-type and Néel-type SkXs have both been investigated thoroughly [26], which can be used to construct two-dimensional magnetic lattices for ultracold atoms. Here, we focus on the Bloch-type SkXs given by Eq. (1), and the Néel-type SkXs can be treated in the same way.

The magnetic field amplitude $\mathcal{B}_c(\mathbf{r})$ generated by the SkX phase in Fig. 1(b) without the external magnetic field $\mathbf{B}$ is shown in Fig. 4(a). Here, $\mathcal{B}_c(\mathbf{r})$ decreases from 105 to 1 mT when the height z increases from 0 to 25 nm; while in the plane at height $z = 5$ nm, $\mathcal{B}_c(\mathbf{r})$ periodically varies from 18 to 40 mT. Specially, the minima of $\mathcal{B}_c(\mathbf{r})$ at a fixed height form a Kagome lattice, while its maxima at the same height form a

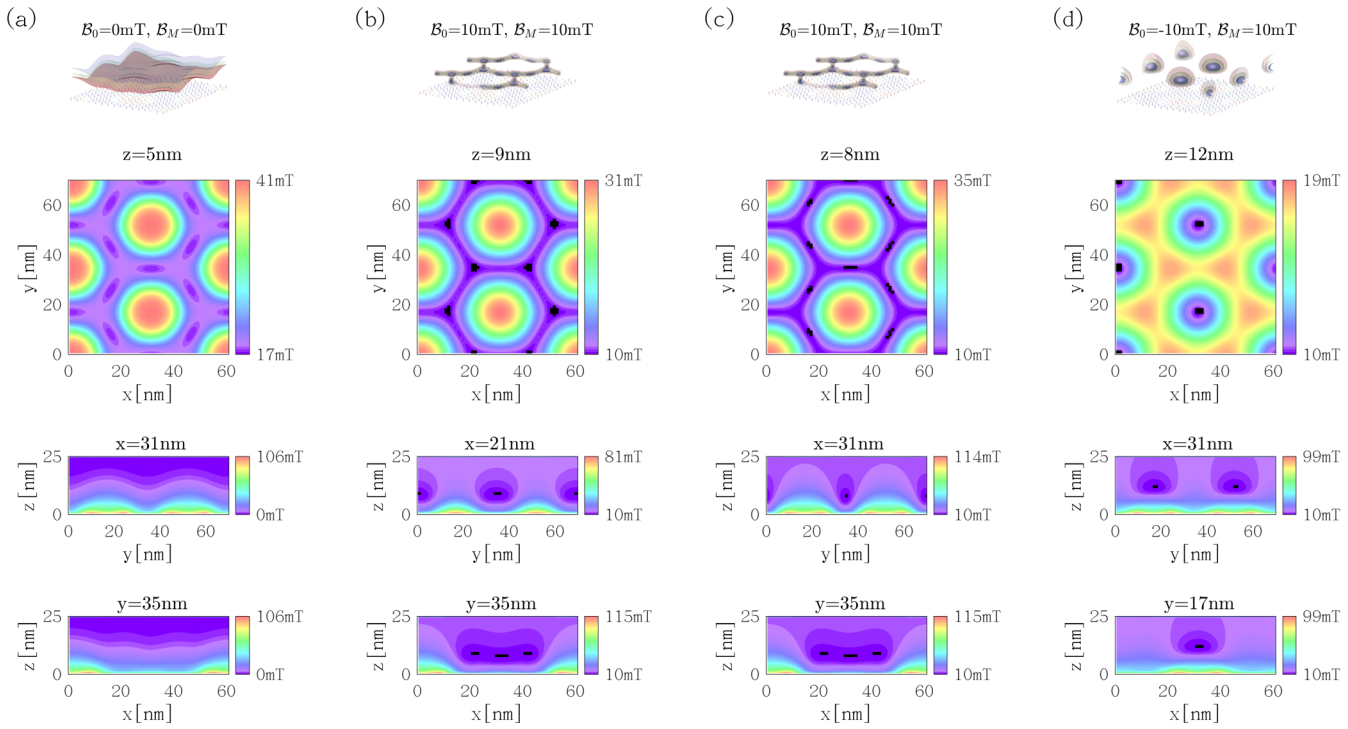

FIG. 4. Profiles of the magnetic field amplitude $\mathcal{B}(\mathbf{r})$ for the chiral ferromagnetic film in the SkX phase. (a) Two-dimensional reflection gating when $\mathcal{B}_0 = 0$ mT and $\mathcal{B}_M = 0$ mT. Top panel: Isosurfaces of $\mathcal{B}(\mathbf{r})$ with three values: 3, 6, and 9 mT. Middle and bottom panels: Cross sections of $\mathcal{B}(\mathbf{r})$ when $z = 5$ nm, $x = 31$ nm, and $y = 35$ nm, respectively. (b) Honeycomb magnetic lattice when $\mathcal{B}_0 = 10$ mT and $\mathcal{B}_M = 10$ mT. Top panel: Isosurfaces of $\mathcal{B}(\mathbf{r})$ with three values: 10.2, 10.4, and 10.6 mT. Middle and bottom panels: Cross sections of $\mathcal{B}(\mathbf{r})$ when $z = 9$ nm, $x = 21$ nm, and $y = 35$ nm, respectively. (c) Kagome magnetic lattice when $\mathcal{B}_0 = 10$ mT and $\mathcal{B}_M = 10$ mT. Top panel: Isosurfaces of $\mathcal{B}(\mathbf{r})$ with three values: 10.2, 10.4, and 10.6 mT. Middle and bottom panels: Cross sections of $\mathcal{B}(\mathbf{r})$ when $z = 8$ nm, $x = 31$ nm, and $y = 35$ nm, respectively. (d) Triangular magnetic lattice when $\mathcal{B}_0 = -10$ mT and $\mathcal{B}_M = 10$ mT. Top panel: Isosurfaces of $\mathcal{B}(\mathbf{r})$ with three values: 11, 12, and 13 mT. Middle and bottom panels: Cross sections of $\mathcal{B}(\mathbf{r})$ when $z = 12$ nm, $x = 31$ nm, and $y = 17$ nm, respectively.

triangular lattice. Therefore, the chiral ferromagnet film in the SkX phase can be viewed as a two-dimensional "reflection grating" for the ultracold atoms.

When the bias magnetic field $\boldsymbol{\mathcal{B}}_0$ and the time-dependent magnetic field $\boldsymbol{\mathcal{B}}_M$ are switched on, the minima of the total magnetic field amplitude $\mathcal{B}(\mathbf{r})$ will appear at finite heights and will form two-dimensional magnetic lattices to trap the ultracold atoms. For example, the distribution of $\mathcal{B}(\mathbf{r})$ when $\mathcal{B}_0 = \mathcal{B}_M = 10$ mT is shown in Figs. 4(b) and 4(c). Here, one group of minimal points appears at the height $z_{\min} = 9$ nm and is located at the centers of the triangles determined by any three nearest skyrmions, and thus form a honeycomb magnetic lattice. Another group of minimal points is located at the middle points between any two nearest skyrmions at the height $z_{\min} = 8$ nm, and thus form a Kagome magnetic lattice. When the direction of the bias magnetic field is reversed with $\mathcal{B}_0 = -10$ mT, a triangular magnetic lattice will be formed at the height $z_{\min} = 12$ nm, and the minimal points of $\mathcal{B}(\mathbf{r})$ will locate at the center of the skyrmions, as shown in Fig. 4(d). The recoil energy E_R now is 1.9 neV for the ^{87}Rb atom and 24 neV for the ^{7}Li atom, where the lattice constant for the SkX phase is about 35 nm.

The magnetization configuration of the Bloch-type SkX is approximately described by a triple-$\mathbf{Q}$ state [23,26]: $\mathbf{m}_{\rm skx}(\mathbf{r}) = \mathbf{m}_0(\mathbf{r})\delta(z) + \mathcal{A}\sum_{i=1}^{3}[\hat{\mathbf{e}}_z \cos(\mathbf{Q}_i \cdot \mathbf{r}) + \hat{\mathbf{e}}_i \sin(\mathbf{Q}_i \cdot \mathbf{r})]\delta(z)$. Without loss of generality, the wave vectors $\mathbf{Q}_i = Q\hat{\mathbf{Q}}_i$ here are set as $\hat{\mathbf{Q}}_1 = (1, 0, 0)$, $\hat{\mathbf{Q}}_2 = (-\frac{1}{2}, \frac{\sqrt{3}}{2}, 0)$, and $\hat{\mathbf{Q}}_3 = (-\frac{1}{2}, -\frac{\sqrt{3}}{2}, 0)$, which then give the set of unit vectors $\hat{\mathbf{e}}_i = \hat{\mathbf{e}}_z \times \hat{\mathbf{Q}}_i$. The spatial distribution of the magnetic field generated by Bloch-type SkXs is explicitly expressed as [26]

$$\boldsymbol{\mathcal{B}}_{\rm skx}(\mathbf{r}) = \frac{\mathcal{A}Q}{2} e^{-Q|z|} \times \begin{pmatrix} \mathrm{sgn}(z)\left[\sin(Qx) + \sin\left(\frac{1}{2}Qx\right)\cos\left(\frac{\sqrt{3}}{2}Qy\right)\right] \\ \mathrm{sgn}(z)\sqrt{3}\cos\left(\frac{1}{2}Qx\right)\sin\left(\frac{\sqrt{3}}{2}Qy\right) \\ \cos(Qx) + 2\cos\left(\frac{1}{2}Qx\right)\cos\left(\frac{\sqrt{3}}{2}Qy\right) \end{pmatrix}. \tag{6}$$

Its modulus is $\mathcal{B}_{\rm skx}(\mathbf{r}) = \frac{\mathcal{A}Q}{2} e^{-Q|z|}\sqrt{\mathcal{F}(x, y)}$, where $\mathcal{F}(x, y) = 1 + 3\cos^2(\frac{1}{2}Qx) + \cos^2(\frac{\sqrt{3}}{2}Qy) + 4\cos^3(\frac{1}{2}Qx)\cos(\frac{\sqrt{3}}{2}Qy)$. We see that $\mathcal{B}_{\rm skx}(\mathbf{r})$ will decay exponentially along with the height $|z|$. Besides, $\mathcal{F}(x, y)$ will reach it minimal value 1 on a Kagome lattice and reach its maximal value 9 on a triangular lattice. Therefore, the analytical results based on the triple-$\mathbf{Q}$ state here coincide with the features revealed numerically in Fig. 4(a).

After turning on the magnetic fields $\mathcal{B}_0 = \frac{\mathcal{A}Q}{2} B_0$ and $\mathcal{B}_M = \frac{\mathcal{A}Q}{2} B_M$, which are weak enough that the SkX phase is not

destroyed, the modulus of the total magnetic field will be $\mathcal{B}(\mathbf{r}) = \frac{AQ}{2}\sqrt{\mathcal{G}(\mathbf{r})}$, where $\mathcal{G}(\mathbf{r}) = B_0^2 + B_M^2 + 2B_0 e^{-Q|z|}[\cos(Qx) + 2\cos(\frac{1}{2}Qx)\cos(\frac{\sqrt{3}}{2}Qy)] + e^{-2Q|z|}\mathcal{F}(x, y)$. Hence, $\mathcal{B}(\mathbf{r})$ will be finite and homogeneously distributed as $|z| \to \infty$, while the minimal value $\mathcal{B}_{\min} = 10$ mT of $\mathcal{B}(\mathbf{r})$ can be achieved at periodic arrays of points at the finite height $z_{\min}$. The minimal points of $\mathcal{B}(\mathbf{r})$ will be determined by

$$\sin\left(\frac{1}{2}Qx\right)\left[2\cos\left(\frac{1}{2}Qx\right) + \cos\left(\frac{\sqrt{3}}{2}Qy\right)\right] = 0,$$

$$\cos\left(\frac{1}{2}Qx\right)\sin\left(\frac{\sqrt{3}}{2}Qy\right) = 0,$$

$$e^{-Q|z|}\left[\cos^2\left(\frac{1}{2}Qx\right) - \sin^2\left(\frac{1}{2}Qx\right) + 2\cos\left(\frac{1}{2}Qx\right)\cos\left(\frac{\sqrt{3}}{2}Qy\right)\right] + B_0 = 0. \quad (7)$$

Three sets of solutions are found for Eq. (7), which then define the following three types of two-dimensional magnetic lattices for the ultracold atoms.

(a) Honeycomb lattice if $0 < B_0 < 3/2$. The lattice sites are defined by $\sin(\frac{1}{2}Qx) = \pm\frac{\sqrt{3}}{2}$, $\cos(\frac{1}{2}Qx) = -\frac{1}{2}$, $\sin(\frac{\sqrt{3}}{2}Qy) = 0$, $\cos(\frac{\sqrt{3}}{2}Qy) = 1$, and $e^{-Q|z|} = \frac{2}{3}\mathcal{B}_0$ or by $\sin(\frac{1}{2}Qx) = \pm\frac{\sqrt{3}}{2}$, $\cos(\frac{1}{2}Qx) = \frac{1}{2}$, $\sin(\frac{\sqrt{3}}{2}Qy) = 0$, $\cos(\frac{\sqrt{3}}{2}Qy) = -1$, and $e^{-Q|z|} = \frac{2}{3}B_0$, as shown in Fig. 5(a). The height of these points is $|z_{\min}| = -\frac{1}{Q}\ln(\frac{2}{3}B_0)$, which will decrease with increased B_0 and vanish at $B_0 = 3/2$. The honeycomb optical lattices have been proposed [34] and shown to trap the ultracold atoms, which then are able to simulate exotic phenomena including the superfluid-to-Mott-insulator transition [35], Dirac points [36], the quantum anomalous Hall effect [37], etc. Therefore, similar physical phenomena of the ultracold atoms are expected when they are trapped by the honeycomb magnetic lattice here.

(b) Kagome lattice if $0 < B_0 < 1$. The lattice sites are defined by $\sin(\frac{1}{2}Qx) = \pm 1$, $\cos(\frac{1}{2}Qx) = 0$, $\sin(\frac{\sqrt{3}}{2}Qy) = \pm 1$, $\cos(\frac{\sqrt{3}}{2}Qy) = 0$, and $e^{-Q|z|} = B_0$; by $\sin(\frac{1}{2}Qx) = 0$, $\cos(\frac{1}{2}Qx) = 1$, $\sin(\frac{\sqrt{3}}{2}Qy) = 0$, $\cos(\frac{\sqrt{3}}{2}Qy) = -1$, and $e^{-Q|z|} = B_0$; or by $\sin(\frac{1}{2}Qx) = 0$, $\cos(\frac{1}{2}Qx) = -1$, $\sin(\frac{\sqrt{3}}{2}Qy) = 0$, $\cos(\frac{\sqrt{3}}{2}Qy) = 1$, and $e^{-Q|z|} = B_0$, as shown in Fig. 5(b). The height of these points is $|z_{\min}| = -\frac{1}{Q}\ln B_0$, which will also decrease with increased B_0 and vanish at $B_0 = 1$. Therefore, the Kagome lattice is more close to the film surface than the honeycomb lattice when the two coexist, which is also revealed in Figs. 4(b) and 4(c). The Kagome lattice has the intriguing ability to host flat band states of ultracold atoms, which is an ideal platform to study quantum many-body physics. Hence, the chiral ferromagnetic film provides a platform to realize the Kagome lattice for ultracold atoms in addition to the optical method [38,39].

(c) Triangular lattice if $-3 < B_0 < 0$. The lattice sites are defined by $\sin(\frac{1}{2}Qx) = 0$, $\cos(\frac{1}{2}Qx) = 1$, $\sin(\frac{\sqrt{3}}{2}Qy) = 0$, $\cos(\frac{\sqrt{3}}{2}Qy) = 1$, and $e^{-Q|z|} = -\frac{1}{3}B_0$ or by $\sin(\frac{1}{2}Qx) = 0$, $\cos(\frac{1}{2}Qx) = -1$, $\sin(\frac{\sqrt{3}}{2}Qy) = 0$, $\cos(\frac{\sqrt{3}}{2}Qy) = -1$, and $e^{-Q|z|} = -\frac{1}{3}B_0$, as shown in Fig. 5(c). The height of these points is $|z_{\min}| = -\frac{1}{Q}\ln(-\frac{1}{3}B_z)$, which will decrease with increased B_0 and vanish at $B_0 = -3$. Similar to the case of the optical lattice, the triangular magnetic lattice here can also be useful to simulate geometrically frustrated magnetism with ultracold atoms [40].

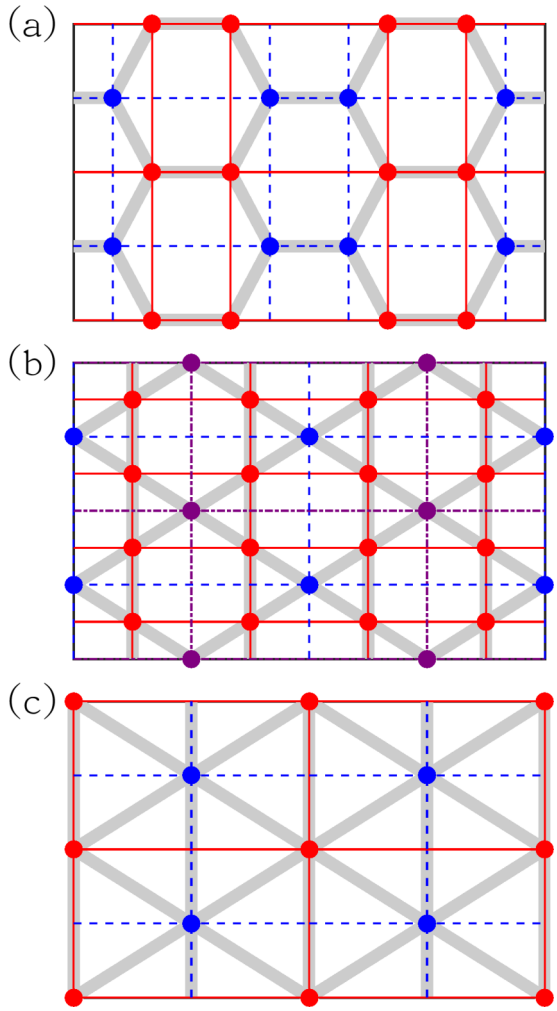

FIG. 5. The sites of three types of two-dimensional magnetic lattices, which are determined by the three sets of solutions of Eq. (7). (a) honeycomb lattice, (b) Kagome lattice, and (c) triangular lattice.

The properties of the two-dimensional magnetic lattices are further investigated for the chiral ferromagnetic film described by Eq. (1). As shown in Fig. 6, the trapping height of each lattice will decrease when the bias magnetic field $\mathcal{B}_0$ is continuously increased with fixed $\mathcal{B}_M = 10$ mT, which agrees with the analytical results above. Meanwhile, the potential barrier U_{barr} for the same type of atom will be the same as the one-dimensional magnetic lattice discussed in Sec. III, since $\delta\mathcal{B}$ only depends on $\mathcal{B}_0$ and $\mathcal{B}_M$. The trapping height and the potential barrier will be the same for the ^{7}Li atom in the state $|F = 2, m_F = 2\rangle$.

The ultracold atoms will be confined in three directions by the two-dimensional magnetic lattices, and the trapping

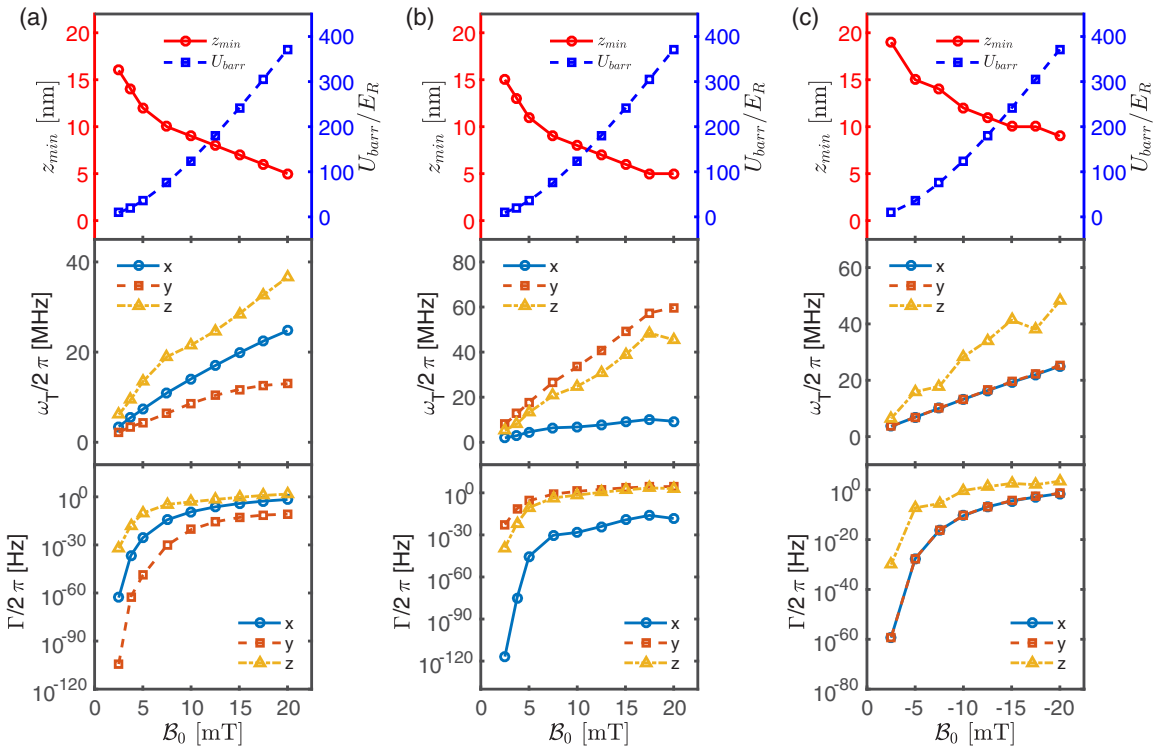

FIG. 6. The dependence of the trapping height $z_{\min}$, the potential barrier U_{barr}, the trapping frequency $\omega_T/2\pi$, and the Majorana loss rate $\Gamma/2\pi$ for the ^{87}Rb atom on the bias magnetic field. Here, E_R is the recoil energy of the ^{87}Rb atom, $\mathcal{B}_0$ varies from 2.5 to 20 mT, and $\mathcal{B}_M$ is fixed as 10 mT. (a) Honeycomb lattice, (b) Kagome lattice, and (c) triangular lattice.

frequencies ω_T for ^{87}Rb atoms are given in Fig. 6 when $\mathcal{B}_M = 10$ mT and $|\mathcal{B}_0|$ varies from 2.5 to 20 mT. Similar to the one-dimensional magnetic lattice, a stronger bias magnetic field will induce higher trapping frequency here. Besides, the inequivalence of trapping frequencies along different directions suggests the anisotropy of the trapping potential near the minima of the two-dimensional magnetic lattices. The Majorana loss rates $\Gamma/2\pi$ for ^{87}Rb atoms in the two-dimensional magnetic lattices are also presented in Fig. 6. As expected, $\Gamma/2\pi$ will be enhanced with increasing the bias magnetic field $\mathcal{B}_0$ and has the same anisotropic feature as the trapping frequency ω_T. Similar to the one-dimensional magnetic lattice, a ^{7}Li atom in the state $|F = 2, m_F = 2\rangle$ will attain higher trapping frequency and larger Majorana loss rate due to its smaller mass.

V. DISCUSSIONS AND CONCLUSION

Although the chiral ferromagnetic film has shown attractive features to control the ultracold atoms, there are still several issues to be addressed for practical performances. First of all, one needs to transfer the ultracold atoms to the magnetic lattices near the film surface for further operations. This might be accomplished by loading the atoms from an external dimple trap [41] by adiabatically tuning the trapping height with the bias field $\mathcal{B}_0$, which in fact has been proposed for the magnetic lattice created by a superconducting film [9]. Second, imperfections will always be introduced to the magnetic field by the unavoidable defects in the chiral ferromagnetic film, such as the bent helical stripes, the irregular array of skyrmions, or even their mixtures [23]. In order to get ideal magnetic lattices, it will be critical to improve the quality of the chiral ferromagnetic film and get perfect magnetic patterns. Finally, the trapping height of the ultracold atoms will be tens of nanometers, which is so close that the Casimir-Polder force between the atoms and the film surface will be significantly enhanced [4]. Therefore, the dynamic behavior of ultracold atoms interacting with the chiral ferromagnetic film should be very different from the case of the optical lattice, which needs to be explored further.

In conclusion, we have investigated the possibility to control ultracold atoms with the magnetic field produced by the chiral ferromagnetic film. We demonstrate how to realize the magnetic mirror, reflection grating, and one-dimensional and two-dimensional magnetic lattices in the proposed device. Compared with current top-down techniques to produce magnetic fields for ultracold atoms, the strategies based on the chiral ferromagnetic film here belong to the bottom-up category and will be more flexible and controllable. With the benefit of the continuous advances of the spintronics technology and material science, the interactive ultracold atoms and the chiral ferromagnetic film can be a promising platform to demonstrate exotic physics phenomena and develop quantum techniques.

ACKNOWLEDGMENTS

This work has been supported by NSFC Projects No. 61674083 and No. 11604162 and by the Fundamental Research Funds for the Central Universities, Nankai University (Grant No. 7540).

[1] C. E. Wieman, D. E. Pritchard, and D. J. Wineland, Rev. Mod. Phys. **71**, S253 (1999).

[2] R. Onofrio, Phys.-Usp. **59**, 1129 (2016).

[3] M. Lewenstein, A. Sanpera, and V. Ahufinger, *Ultracold Atoms in Optical Lattices : Simulating Quantum Many-Body Systems* (Oxford University, Oxford, 2012).

[4] *Atom Chips*, edited by J. Reichel and V. Vuletić (Wiley VCH, Berlin, 2011).

[5] J. Fortágh and C. Zimmermann, Rev. Mod. Phys. **79**, 235 (2007).

[6] R. Gerritsma, S. Whitlock, T. Fernholz, H. Schlatter, J. A. Luigjes, J.-U. Thiele, J. B. Goedkoop, and R. J. C. Spreeuw, Phys. Rev. A **76**, 033408 (2007).

[7] Y. Wang, T. Tran, P. Surendran, I. Herrera, A. Balcytis, D. Nissen, M. Albrecht, A. Sidorov, and P. Hannaford, Phys. Rev. A **96**, 013630 (2017).

[8] T. Müller, B. Zhang, R. Fermani, K. S. Chan, Z. W. Wang, C. B. Zhang, M. J. Lim, and R. Dumke, New J. Phys. **12**, 043016 (2010).

[9] O. Romero-Isart, C. Navau, A. Sanchez, P. Zoller, and J. I. Cirac, Phys. Rev. Lett. **111**, 145304 (2013).

[10] X. Luo, L. Wu, J. Chen, R. Lu, R. Wang, and L. You, New J. Phys. **17**, 083048 (2015).

[11] J. Yu, Z.-F. Xu, R. Lü, and L. You, Phys. Rev. Lett. **116**, 143003 (2016).

[12] A. D. West, K. J. Weatherill, T. J. Hayward, P. W. Fry, T. Schref, M. R. J. Gibbs, C. S. Adams, D. A. Allwood, and I. G. Hughes, Nano. Lett. **12**, 4065 (2012).

[13] I. Dzyaloshinskii, J. Phys. Chem. Solids **4**, 241 (1958).

[14] T. Moriya, Phys. Rev. **120**, 91 (1960).

[15] R. Wiesendanger, Nat. Rev. Mater. **1**, 16044 (2016).

[16] A. Fert, N. Reyren, and V. Cros, Nat. Rev. Mater. **2**, 17031 (2017).

[17] A. N. Bogdanov and U. K. Rößler, Phys. Rev. Lett. **87**, 037203 (2001).

[18] U. K. Rößler, A. N. Bogdanov, and C. Pfleiderer, Nature (London) **442**, 797 (2006).

[19] S. Mühlbauer, B. Binz, F. Jonietz, C. Pfleiderer, A. Rosch, A. Neubauer, R. Georgii, and P. Böni, Science **323**, 915 (2009).

[20] X. Z. Yu, Y. Onose, N. Kanazawa, J. H. Park, J. H. Han, Y. Matsui, N. Nagaosa, and Y. Tokura, Nature (London) **465**, 901 (2010).

[21] X. Z. Yu, N. Kanazawa, Y. Onose, K. Kimoto, W. Z. Zhang, S. Ishiwata, Y. Matsui, and Y. Tokura, Nat. Mater. **10**, 106 (2010).

[22] S. Heinze, K. von Bergmann, M. Menzel, J. Brede, A. Kubetzka, R. Wiesendanger, G. Bihlmayer, and S. Blügel, Nat. Phys. **7**, 713 (2011).

[23] N. Nagaosa and Y. Tokura, Nat. Nanotechnol. **8**, 899 (2013).

[24] W. Kang, Y. Huang, X. C. Zhang, Y. Zhou, and W. Zhao, Proc. IEEE **104**, 2040 (2016).

[25] Y. Dovzhenko, F. Casola, S. Schlotter, G. S. D. Beach, and A. Yacoby, Nat. Commun. **9**, 2712 (2018).

[26] R. Qin and Y. Wang, New J. Phys. **20**, 063029 (2018).

[27] W. Petrich, M. H. Anderson, J. R. Ensher, and E. A. Cornell, Phys. Rev. Lett. **74**, 3352 (1995).

[28] R. Wang, M. Liu, F. Minardi, and M. Kasevich, Phys. Rev. A **75**, 013610 (2007).

[29] E. A. Hinds and I. G. Hughes, J. Phys. D: Appl. Phys. **32**, R119 (1999).

[30] K. Shibata, X. Z. Yu, T. Hara, D. Morikawa, N. Kanazawa, K. Kimoto, S. Ishiwata, Y. Matsui, and Y. Tokura, Nat. Nanotechnol. **8**, 723 (2013).

[31] K. Shibata, J. Iwasaki, N. Kanazawa, S. Aizawa, T. Tanigaki, M. Shirai, T. Nakajima, M. Kubota, M. Kawasaki, H. S. Park, D. Shindo, N. Nagaosa, and Y. Tokura, Nat. Nanotechnol. **10**, 589 (2015).

[32] D. M. Brink and C. V. Sukumar, Phys. Rev. A **74**, 035401 (2006).

[33] H. Oike, A. Kikkawa, N. Kanazawa, Y. Taguchi, M. Kawasaki, Y. Tokura, and F. Kagawa, Nat. Phys. **12**, 62 (2016).

[34] K. L. Lee, B. Grémaud, R. Han, B.-G. Englert, and C. Miniatura, Phys. Rev. A **80**, 043411 (2009).

[35] P. Soltan-Panahi, J. Struck, P. Hauke, A. Bick, W. Plenkers, G. Meineke, C. Becker, P. Windpassinger, M. Lewenstein, and K. Sengstock, Nat. Phys. **7**, 434 (2011).

[36] L. Tarruell, D. Greif, T. Uehlinger, G. Jotzu, and T. Esslinger, Nature (London) **483**, 302 (2012).

[37] G. Jotzu, M. Messer, R. Desbuquois, M. Lebrat, T. Uehlinger, D. Greif, and T. Esslinger, Nature (London) **515**, 237 (2014).

[38] J. Ruostekoski, Phys. Rev. Lett. **103**, 080406 (2009).

[39] G.-B. Jo, J. Guzman, C. K. Thomas, P. Hosur, A. Vishwanath, and D. M. Stamper-Kurn, Phys. Rev. Lett. **108**, 045305 (2012).

[40] J. Struck, C. Ölschläger, R. Le Targat, P. Soltan-Panahi, A. Eckardt, M. Lewenstein, P. Windpassinger, and K. Sengstock, Science **333**, 996 (2011).

[41] D. M. Stamper-Kurn, H.-J. Miesner, A. P. Chikkatur, S. Inouye, J. Stenger, and W. Ketterle, Phys. Rev. Lett. **81**, 2194 (1998).